Spatially variable geothermal heat flux in West Antarctica: evidence and implications

Carolyn Branecky Begeman[1], Slawek M. Tulaczyk[1], and Andrew T. Fisher[1]

[1]Department of Earth and Planetary Sciences, University of California, Santa Cruz, Santa Cruz, CA, USA.

Corresponding author: Carolyn Branecky Begeman (cbranecky@ucsc.edu)

Key Points:

- Measured geothermal flux at the grounding zone of the Whillans Ice Stream is 88 ± 7 mW m^{-2}, higher than the average continental flux.
- West Antarctica exhibits high spatial variability in geothermal flux, consistent with local magmatic intrusions or crustal fluid advection.
- Spatial variability in geothermal flux exceeds spatial variability in the conductive heat flux through ice along the Siple Coast.

Abstract

Geothermal heat flux (GHF) is an important part of the basal heat budget of continental ice sheets. The difficulty of measuring GHF below ice sheets has directly hindered progress in understanding of ice sheet dynamics. We present a new GHF measurement from below the West Antarctic Ice Sheet, made in subglacial sediment near the grounding zone of the Whillans Ice Stream. The measured GHF is 88 ± 7 mW m^{-2}, a relatively high value compared to other continental settings and to other GHF measurements along the eastern Ross Sea of 55 mW m^{-2} and 69 ± 21 mW m^{-2}, but within the range of regional values indicated by geophysical estimates. The new GHF measurement was made ~100 km from the only other direct GHF measurement below the ice sheet, which was considerably higher at 285 ± 80 mW m^{-2}, suggesting spatial variability that could be explained by shallow magmatic intrusions or the advection of heat by crustal fluids. Analytical calculations suggest that spatial variability in GHF exceeds spatial variability in the conductive heat flux through ice along the Siple Coast. Accurate GHF measurements and high-resolution GHF models may be necessary to reliably predict ice sheet evolution, including responses to ongoing and future climate change.

This article has been accepted for publication and undergone full peer review but has not been through the copyediting, typesetting, pagination and proofreading process which may lead to differences between this version and the Version of Record. Please cite this article as doi: 10.1002/2017GL075579

1 Introduction

Geothermal heat flux (GHF) is a significant source of heat in polar subglacial environments. It affects the temperature at the base of ice sheets, impacting the ice sheet mass balance directly through basal melting or freezing. GHF can have a large indirect effect on ice sheet mass balance when it brings the basal temperature above the melting point because the presence of basal meltwater reduces basal resistance, facilitating fast sliding of ice [*Weertman*, 1964]. GHF is prescribed as part of the lower boundary conditions for ice sheet models, which calculate patterns of basal melting and freezing to determine the degree of ice sliding. Ice sheet models are sensitive to the magnitude and spatial variability of GHF, particularly when the GHF contribution shifts basal temperatures across the melting point [*Bougamont et al.*, 2015; *Pittard et al.*, 2016].

Despite the importance of GHF below ice sheets, there are relatively few direct measurements of this key parameter [*Davies and Davies*, 2010], mainly because it is so difficult to access the subglacial environment. Prior to this study, the only direct GHF measurement below the WAIS was made at Subglacial Lake Whillans (SLW) [*Fisher et al.*, 2015]; estimates were made at two additional locations using basal ice temperatures and assumptions about local ice dynamics [*Engelhardt*, 2004a; *Clow et al.*, 2012]. GHF has been inferred for some regions of the WAIS from the distribution of subglacial water [*Siegert and Dowdeswell*, 1996; *Schroeder et al.*, 2014]. Due to the paucity of observations, the GHF distribution used in ice sheet models typically falls within a relatively narrow range and has low spatial variability, based on geological or remotely-sensed properties of the underlying lithosphere [*Pollack et al.*, 1993; *Shapiro and Ritzwoller*, 2004; *Maule*, 2005; *An et al.*, 2015; *Burton-Johnson et al.*, 2017]. GHF models of West Antarctica are inconsistent with one another in both magnitude and distribution (Fig. S1), suggesting that GHF is not well constrained.

2 Materials and Methods

We determined the GHF 3 km downstream of the Whillans ice stream Grounding Zone (WGZ) using an ice borehole to collect measurements of thermal gradient and thermal conductivity.

2.1 Temperature gradient in sediments

The ice drilling operations are described in Tulaczyk *et al.* [2014]. The geothermal probe used to measure the thermal gradient is the same tool used at SLW [*Fisher et al.*, 2015]. For the present study, the geothermal probe was deployed twice, on 15 January 2015 and 18 January 2015, resulting in a horizontal distance of 3 m between measurements due to ice movement. The probe makes subsurface measurements with three autonomous sensor/logger systems, with sensor spacing of 62 cm. Autonomous sensors/loggers were calibrated before deployment with absolute accuracy of ±0.002°C [*Fisher et al.*, 2015]. The sensors/loggers were programmed just before deployment for synchronous data collection every 2s. After data were recovered, and calibration corrections were applied, we performed an additional shift to individual sensors (0.003 – 0.008°C) based on measurements made when the geothermal probe was held stationary in the water column (Fig. S2). This is the routine approach for GHF measurements in the deep sea, and assures that small variations in apparent temperature (generally due to electronic drift) do not bias geothermal data.

After the probe was inserted into the sediment at WGZ, it was held still for ~10 minutes to record the transient temperature response. Data from this measurement period for each sensor were fitted to a conductive heat flow model of temperature equilibration [*Bullard*, 1954] using TP-Fit software [*Heesemann et al.*, 2006]. The modeled equilibration

period started ~100 s after penetration, to avoid deviations from the idealized model used to fit the data (a thin line source), and lasted 5-8 minutes. Processing of the data was managed sensor by sensor, with care taken to avoid data intervals that included evidence for probe motion, expressed as frictional heating that lead to subtle deviations in the standard equilibration curve. Data processing was completed with thermal conductivity values that are consistent with measurements described in section 2.2. Equilibration of conventional oceanographic heat flow probes often takes longer than the usual 6-7 minute measurement window [*Davis and Fisher*, 2011], but the geothermal sensor/logger systems used in this study have sensors mounted within 5-mm outer diameter stainless steel tubing, which equilibrates quickly with surrounding material. Because of this, sensors were nearly equilibrated by the end of the useful measurement window, and extrapolation to full equilibration was relatively insensitive to model parameters (thermal conductivity, thermal diffusivity, time shift to improve model fit). The greatest source of uncertainty in equilibrium temperature (0.001-0.006 °C) came from selection of alternative measurement windows used for extrapolation to *in-situ* conditions.

2.2 Thermal conductivity

Sediment was recovered with a gravity corer in a 5.5 cm diameter polycarbonate liner through the same borehole adjacent to the thermal gradient measurements (sediment core WGZ-GC-1). Thermal conductivity, *k*, was measured in the laboratory on a 55 cm section of this core, using the needle probe method [*Von Herzen and Maxwell*, 1959], with measurements made every 1 cm for 40 cm. For each measurement, we drilled a 1.6-mm-diameter hole through the core liner, stopping before penetrating the core itself. We placed a 5-cm-long needle probe, containing a thermistor and heater wire, through the hole and into the sediment, perpendicular to the axis of the core. Constant heating was applied, and the temperature rise during the first 10 to 50 s followed a consistent ln(time) trend and was used for interpretation. The standard deviation of individual *k* values, based on fitting of data to a model of line-source heating, was ±0.0025 $Wm^{-1}°C^{-1}$, and tests made with the same sized core liner filled with water solidified by gelatin yielded values consist with water ±5%. We interpret individual *k* values measured with the needle probe to have an uncertainty of ±5%, and applied corrections for the difference between core and laboratory temperatures, an adjustment of –0.193% $°C^{-1}$ [*Morin and Silva*, 1984]. The effective conductivity of the core was calculated as the harmonic mean (± standard deviation of measurements), which is appropriate for vertical heat conduction through a heterogeneously layered system [*Bullard*, 1939]. This calculation is dominated by conductivity values on the lower end of the measured range, so is conservative when calculating the vertical heat flux, which is the product of thermal gradient and thermal conductivity. We applied a geometric mean model for a two-phase media of solid and fluid to calculate apparent trends in sediment porosity from thermal conductivity data [*Brigaud and Vasseur*, 1989].

2.3 Grain size

Since variations in grain size can influence the thermal conductivity of sediments [*Gangadhara Rao and Singh*, 1999], we analyzed sediment samples to determine grain size, using the same core for which we measured thermal conductivity, in 1 cm depth increments. Grains with diameters <1 mm were analyzed with a laser-diffraction, particle size analyzer (PSA). The PSA uses light scattering to quantify particle size distribution within a liquid suspension, using a 5 mW laser source having a 750-nm wavelength. Samples were suspended in an eluent containing 0.1 g/L of sodium metaphosphate to deflocculate small particles, and circulated continuously during measurement. The result for each sample is a

probability density function of grain sizes within 93 logarithmically-scaled bins ranging from <0.4 μm to <1 mm (Fig. S4). To determine size fractions >1 mm which could not be analyzed with the PSA, samples were cut from the core and wet-sieved to isolate 1–2 mm and >2 mm diameter size classes, which were weighed (Fig. S5). Results from the sieve and PSA methods were combined for each sample, assuming consistent grain density in the coarse and fine fractions.

2.4 Spatial variability in other heat flux terms at the ice sheet bed

To place the observed GHF variations in the context of other factors influencing the basal thermal energy balance of the ice sheet, we offer basal heat flux estimates characteristic of the Siple Coast. To solve for the vertical conductive heat flux into the ice, q_i, we use the analytical solution of Robin [1955] for the 1-D thermal advection-diffusion equation. This solution assumes that the vertical velocity v_z decreases linearly from the accumulation rate at the surface to 0 at the ice sheet base (Text S2, Fig. S6). We consider the steady-state case for an ice sheet in mass balance to gain insight into the most important terms in the basal thermal energy balance. We take the derivative of the Robin [1955] solution, to yield the temperature gradient at the base of the ice, $dT/dz|_b$, and multiply by the thermal conductivity of ice, k_i, to solve for q_i:

$$q_i = k_i \frac{dT}{dz}\Big|_b = k_i \frac{2(T_b - T_s)\sqrt{P/2}}{h\sqrt{\pi}\, erf\left(\sqrt{P/2}\right)} \quad (1).$$

T_b and T_s are the temperature at the base and surface of the ice sheet, respectively; h is the ice thickness; and P is the Peclet number, the ratio of thermal advection to diffusion, calculated as $ah\kappa^{-1}$ where a is the accumulation rate and κ is the thermal diffusivity. k_i is calculated as a function of temperature [*Cuffey and Paterson*, 2010].

In these calculations, we assume T_b is at the pressure melting point, $T_m(p)$, the maximum basal temperature for a frozen bed. Thus, these q_i such that $T_b$solutions represent a local upper bound on the vertical conductive heat flux through ice. $T_m(p)$ is calculated using freshwater properties [*IOC et al.*, 2010] and p is calculated as a function of ice thickness with an average ice density of 900 kg m^{-3} to account for the effects of air bubbles and firn.

Calculated q_i values depend mainly on three independent variables: ice thickness [*Fretwell et al.*, 2013], ice accumulation rate [*Arthern et al.*, 2006; *van de Berg et al.*, 2006], and mean annual surface temperature [*Comiso*, 2000] (error estimates in Table S6, sensitivity analysis in Fig. S7). To illustrate the contribution of variability in each of these factors to variability in q_i, we present calculations of q_i along a profile near the Ross Ice Shelf grounding line, varying one factor while holding the rest at their average value across that profile ($\bar{a}$ = 12 cm yr^{-1}, $\bar{h}$ = 800 m, $\bar{T_s}$ = -21 °C).

We also present an estimate of heat production by friction between the ice sheet base and the subglacial stratum. This shear heating is the product of basal velocity and basal drag along flow. Yield strengths of till collected below the Whillans Ice Stream are a few kPa [*Tulaczyk et al.*, 2000]. Thus, the basal velocity approaches the surface velocity. In this calculation of the shear heat flux, we take basal velocity equal to the surface velocity, representing an upper bound on the shear heat flux. Since basal drag is poorly-constrained, we calculate shear heat flux profiles using a range of basal drag values from 2 to 10 kPa.

Although we do not account for heat sources and sinks due to freezing or melting and heat advection due to subglacial water flow, these are consistent with our calculated q_i, which is an upper bound given $T_b = T_m(p)$. This analytical approach neglects lateral ice advection, which may alter q_i within ice streams if lateral gradients in surface ice temperature are significant. However, along the Siple Coast surface temperature gradients are small [*Comiso*, 2000], and this analytical approach reproduces the ice temperature profile reasonably well at

SLW [*Fisher et al.*, 2015]. A more thorough analysis of this source of variability would entail 3-D ice sheet modeling.

3 Results and Discussion

3.1 GHF observations

Two measurements of the thermal gradient at the WGZ show good agreement, yielding a temperature gradient of 0.050 ± 0.004 °C m^{-1} (mean ± S.D.) (Fig. 1; for the full record, see Fig. S2 and Data Set S1). The thermal conductivity (*k*) of sediments collected at the site range from 1.6 to 2.1 W $m^{-1}°C^{-1}$, with local variations that are likely associated with differences in grain size [*Gangadhara Rao and Singh*, 1999] (Fig. S4), grain lithology, and/or porosity [*Brigaud and Vasseur*, 1989] (Fig. 1c, Data Set S2). There is no clear trend in *k* with depth, and we use the harmonic mean of measured *k* values, 1.77 ± 0.15 W $m^{-1}°C^{-1}$, to calculate GHF.

At the WGZ, the vertical, conductive GHF is 88 ± 7 mW m^{-2} (mean ± 1 S.E., Table S1). The shallowest equilibrium sediment temperatures have the largest uncertainties (Fig. 2b), perhaps because of disruption of shallow sediments by probe insertion. If these data are omitted, then the geothermal gradient is ~18% greater, and GHF is 104 ± 3 mW m^{-2}. In contrast, the same tools and methods were applied at SLW, ~100 km away, yielding GHF of 285 ± 80 mW/m^2 [*Fisher et al.*, 2015]. An earlier measurement below the Ross Ice Shelf at J9, ~200 km from the WGZ, indicated GHF of 55 mW m^{-2} (Fig. 2) [*Foster*, 1978].

3.2 Processes contributing to elevated and variable GHF in West Antarctica

There are a number of factors that can contribute to elevated and/or variable GHF, acting over a range of length scales (Table 1). We examine each of these factors to determine which could explain large variations in GHF (200 mW m^{-2}) over relatively short distances (≤100 km), as observed below the Whillans Ice Stream. The spatial scales of crustal thickness variability are too broad and the magnitude of resulting GHF deviations too small to explain the observed GHF variability [*Fox Maule et al.*, 2005; *Chaput et al.*, 2014] (Text S1c, Fig 3a). Thermal conductivity variability can produce small-scale GHF variability by conductive refraction, but the maximum difference in GHF is 30 mW m^{-2} (Text S1a). While variability in crustal radiogenic heat production can produce small-scale GHF variability as well, it is unlikely to enhance GHF by more than 18 mW m^{-2} (Fig. 2a, Text S1b) [*Vilà et al.*, 2010]. Erosion and lithospheric extension in West Antarctica produce small rates of vertical advection that enhance GHF by ≤10 mW m^{-2} (Text S1d,e) [*Lachenbruch*, 1978; *Mancktelow and Grasemann*, 1997].

Two remaining processes could generate the observed spatial variability in GHF: (a) recent magmatism at shallow crustal depths, and/or (b) advection of heat by crustal fluid flow, potentially associated with hydrothermal circulation. The influence of magmatic intrusions on GHF is estimated using the analytical, transient solution of Lachenbruch *et al.* [1976] for a prismatic intrusion (Fig. 2b). In this model, the thermal conductivity of the surrounding crust is homogeneous and set to 2.8 W m^{-1} $°C^{-1}$, the initial temperature of the intrusion is set to 1000°C, and the background GHF at the surface outside of the influence of the intrusion is set to 70 mW m^{-2}. GHF values in excess of 200 mWm^{-2} are reached as a result of intrusions <5 km in diameter emplaced within the last 150 kyr. These intrusions can generate elevated GHF with spatial footprints less than 10 km [*Lachenbruch et al.*, 1976]. Geophysical observations have been interpreted as indicating extensive magmatism within the West Antarctic Rift System (WARS) [*Behrendt et al.*, 1994; *Trey et al.*, 1999; *Decesari et al.*, 2007; *An et al.*, 2015], including volcanism within the last several decades [*Blankenship*

et al., 1993; *Corr and Vaughan*, 2008; *Lough et al.*, 2013]. Magmatic intrusions in the lower crust are thought to cause geothermal gradients of 50-100 °C km^{-1} in McMurdo Volcanic Province [*Berg et al.*, 1989] (Fig. S9), a range that overlaps with the geothermal gradient of 91-162 °C km^{-1} measured at SLW [*Fisher et al.*, 2015].

The flow of crustal fluids can also increase GHF within a broad area or redistribute heat locally, depending on fluid pathways, flow rates, and the depth of circulation [*Fisher and Harris*, 2010]. Hydrothermal circulation in basement rocks, even below sediments, can generate GHF anomalies with spatial scales of several to tens of kilometers [e.g., *Fisher et al.*, 1990; *Davis et al.*, 1997]. Vigorous local convection can lead to isothermal conditions in a buried aquifer, resulting in large differences in GHF (several hundred mW m^{-2}) through overlying strata as a function of depth to the aquifer top [*Davis et al.*, 1997; *Spinelli and Fisher*, 2004]. Where basement is exposed at the base of the ice, it may provide a conduit for discharge and recharge of hydrothermal fluids, increasing and decreasing GHF, respectively [e.g., *Davis et al.*, 1992; *Villinger et al.*, 2002; *Fisher et al.*, 2003]. The magnitude of GHF anomalies where basement outcrops at the surface can be several W m^{-2}, relative to background values of ~100 mW m^{-2} [e.g., *Davis et al.*, 1992; *Villinger et al.*, 2002; *Fisher et al.*, 2003]. The gravity data collected at WGZ suggests that basement topography may exist [*Muto et al.*, 2013], but there is no such evidence at SLW. The gravity data is consistent with a crustal fault, which could enhance permeability by several orders of magnitude relative to unfaulted bedrock [*Seront et al.*, 1998], focusing vertical fluid advection and elevating GHF. Thus, either magmatism or advection of heat by fluids may contribute to high and spatially-variable GHF in West Antarctica.

These two processes have also played a role in generating GHF variability in other rift systems [*Reiter et al.*, 1975]. The observed variability of the GHF in West Antarctica is consistent with that of other rift systems [*Davies and Davies*, 2010] such as the Basin and Range Province of North America, which is often considered to be a geologic analog for the WARS in terms of the scale, degree of extension, and present crustal thickness [*Coney and Harms*, 1984; *Trey et al.*, 1999]. Currently available GHF constraints are consistent with the broad distribution of GHF values in the Basin and Range Province, 16% of which exceed 300 mW m^{-2} (Fig. 3c). The apparent spatial correlation between rift basins and ice streams in West Antarctica [*Anandakrishnan et al.*, 1998; *Decesari et al.*, 2007; *Bingham et al.*, 2012] suggests that rifting-related processes such as magmatism or preferential advection of crustal fluids may affect ice dynamics by enhancing GHF.

3.3 Implications of high and variable GHF for slow-flowing ice

Given that GHF measurements reveal a wide range of variability, from tens of mW m^{-2} over distances of ~200 km (WGZ, J9, SD) to ~200 mW m^{-2} over ~100 km (WGZ, SLW), we compare this variability with independent estimates for the variability in heat flux on the Siple Coast (Fig. 2b).

Estimated lateral variations in the vertical conductive heat flux are dominated by spatial variations in ice thickness. Calculated fluxes increase by 7 mW m^{-2} per 100 m decrease in ice thickness, resulting in spatial variations of 7-28 mW m^{-2} over 100 km from interstream ridge to ice stream trough. In contrast, estimated lateral variations in the vertical conductive heat flux due to changes in accumulation rate are generally <10 mW m^{-2} per 100 km. Estimated lateral variations in the vertical conductive heat flux due to changes in surface temperature are generally <5 mW m^{-2} per 100 km. The frictional heat flux due to ice sliding over subglacial sediments is poorly-constrained due to uncertainties in basal resistance and basal sliding velocity, but is estimated to be <125 mW m^{-2} near WGZ where ice velocity is around 300 m yr^{-1}. These sources of variability in heat flux are less than the spatial variability

in GHF of ~200 mW m^{-2} per 100 km (WGZ, SLW) and of the same magnitude as the spatial variability between other GHF estimates (WGZ, J9, SD).

4 Conclusions

Current geophysical GHF models underestimate the observed magnitude and spatial variability of GHF, which may be enhanced by magmatism or advection of crustal fluids. Large differences in sea level rise predictions from Antarctica result from two GHF models with narrow GHF distributions [*Bougamont et al.*, 2015]. The observed spatial variability in GHF raises the possibility that GHF plays a greater role in ice dynamics than generally considered. Zones of elevated GHF below the WAIS can produce considerable volumes of subglacial meltwater [*Vogel and Tulaczyk*, 2006] and may contribute to the development and dynamics of subglacial lakes, the advection of organic and inorganic compounds into subglacial habitats, and thus the presence and metabolism of microbial biomes [*Jørgensen and Boetius*, 2007; *Christner et al.*, 2014]. Seroussi *et al.* [2017] found that locally high GHF (≥150 mW m^{-2}) below the Whillans Ice Stream was needed to reproduce the observed subglacial lakes in an ice sheet model. As the ice sheet thins, increasing the vertical conductive heat flux, GHF variability may be more important to predictions of the basal thermal regime, particularly the development of basal frozen zones such as ice rises that might stabilize ice retreat [*Rignot et al.*, 2004; *Favier and Pattyn*, 2015].

Bed topography and ice sheet thickness are relatively well-constrained for much of West Antarctica [*Fretwell et al.*, 2013]. Spatial variability in GHF may contribute more to the uncertainty in the basal thermal regime of West Antarctica than does the remaining uncertainty in ice thickness, which is equivalent to GHF uncertainty of 4 mW m^{-2} along the Siple Coast (Table S6). More direct GHF observations are needed to constrain continental GHF models. Ice sheet modeling could direct GHF observations to locations where future ice sheet mass balance is most sensitive to GHF, to maximize the impact of field measurements. Until such observational constraints become available, we recommend running ensembles of ice sheet models for multiple spatial distributions of GHF below the WAIS, including distributions as broad as that in the Basin and Range Province, to set more realistic limits on rates of ice loss.

Acknowledgments, Samples, and Data

Geothermal heat flux measurements were supported by the US National Science Foundation, Section for Antarctic Sciences, Antarctic Integrated System Science program as part of the interdisciplinary WISSARD (Whillans Ice Stream Subglacial Access Research Drilling) project. The drilling team from University of Nebraska–Lincoln, the WISSARD traverse personnel, the U.S. Antarctic Program, and Air National Guard and Kenn Borek Air provided technical and logistical support. D. Thayer, D. Smith, and S. Ornellas were the primary builders of the geothermal probe. T. Sproule collaborated on geothermal probe thermistor calibration. D. van den Dries assisted in the analysis of sediment core WGZ-GC-1. This work was supported by awards from the U.S. National Science Foundation as part of the WISSARD project, NSF grants ANT-1346251, ANT-0838947, ANT-0839142, OCE-0939564, OCE-1260408, an NSF Graduate Research Fellowship. This is C-DEBI contribution XX.

The authors declare no competing financial interests.

The geothermal heat flux and thermal conductivity measurements are available in the Global Heat Flow Database, [doi to be inserted after acceptance], and Data Sets S1 and S2. Grain size data are available in the EarthChem Library, [doi to be inserted after acceptance], and Data Set S2. The vertical conductive flux estimates are available in figshare with the

identifier 10.6084/m9.figshare.5414062. The authors declare that all other data supporting the findings of this study are available within the paper and its supplementary data files. The methods used to analyze sediment core WGZ-GC-1 were destructive, so samples are not available for further analysis. The following datasets were used in this study: bed elevation available at https://nsidc.org/data/docs/daac/nsidc0422_antarctic_1km_dem/, ice thickness available at https://legacy.bas.ac.uk//bas_research/data/access/bedmap/database/, accumulation and mean annual surface temperature available at http://websrv.cs.umt.edu/isis/index.php/Present_Day_Antarctica, and GHF data from the Basin and Range Province available at http://geothermal.smu.edu/gtda/.

References

An, M., D. A. Wiens, Y. Zhao, M. Feng, A. Nyblade, M. Kanao, Y. Li, A. Maggi, and J.-J. Lévêque (2015), Temperature, lithosphere-asthenosphere boundary, and heat flux beneath the Antarctic Plate inferred from seismic velocities, *J. Geophys. Res. Solid Earth*, *120*(12), doi:10.1002/2015JB011917.

Anandakrishnan, S., D. D. Blankenship, R. B. Alley, and P. L. Stoffa (1998), Influence of subglacial geology on the position of a West Antarctic ice stream from seismic observations, *Nature*, *394*(6688), 62–65, doi:10.1038/27889.

Anandakrishnan, S., and J. P. Winberry (2004), Antarctic subglacial sedimentary layer thickness from receiver function analysis, *Glob. Planet. Change*, *42*(1–4), 167–176, doi:10.1016/j.gloplacha.2003.10.005.

Armienti, P., and C. Perinelli (2010), Cenozoic thermal evolution of lithospheric mantle in northern Victoria Land (Antarctica): Evidences from mantle xenoliths, *Tectonophysics*, *486*(1–4), 28–35, doi:10.1016/j.tecto.2010.02.006.

Bamber, J. L., J. L. Gomez-Dans, and J. A. Griggs (2009), *Antarctic 1 km Digital Elevation Model (DEM) from Combined ERS-1 Radar and ICESat Laser Satellite Altimetry*, Digital media, National Snow and Ice Data Center, Boulder, Colorado USA.

Behrendt, J. C., D. D. Blankenship, C. A. Finn, R. E. Bell, R. E. Sweeney, S. M. Hodge, and J. M. Brozena (1994), CASERTZ aeromagnetic data reveal late Cenozoic flood basalts(?) in the West Antarctic rift system, *Geology*, *22*(6), 527–530, doi:10.1130/0091-7613(1994)022<0527:CADRLC>2.3.CO;2.

Berg, J. H., R. J. Moscati, and D. L. Herz (1989), A petrologic geotherm from a continental rift in Antarctica, *Earth Planet. Sci. Lett.*, *93*(1), 98–108, doi:10.1016/0012-821X(89)90187-8.

Bindschadler, R. A., E. P. Roberts, and A. Iken (1990), Age of Crary Ice Rise, Antarctica, determined from temperature-depth profiles, *Ann. Glaciol.*, *14*, 13–16.

Bingham, R. G., F. Ferraccioli, E. C. King, R. D. Larter, H. D. Pritchard, A. M. Smith, and D. G. Vaughan (2012), Inland thinning of West Antarctic Ice Sheet steered along subglacial rifts, *Nature*, *487*(7408), 468–471, doi:10.1038/nature11292.

Blankenship, D. D., R. E. Bell, S. M. Hodge, J. M. Brozena, J. C. Behrendt, and C. A. Finn (1993), Active volcanism beneath the West Antarctic ice sheet and implications for ice-sheet stability, *Nature*, *361*(6412), 526–529, doi:10.1038/361526a0.

Bougamont, M., P. Christoffersen, S. F. Price, H. A. Fricker, S. Tulaczyk, and S. P. Carter (2015), Reactivation of Kamb Ice Stream tributaries triggers century-scale reorganization of Siple Coast ice flow in West Antarctica: Restructuring of Siple Coast ice flow, *Geophys. Res. Lett.*, *42*(20), 8471–8480, doi:10.1002/2015GL065782.

Bredehoeft, J. D., and I. S. Papadopulos (1965), Rates of vertical groundwater movement estimated from the Earth's thermal profile, *Water Resour. Res.*, *1*(2), 325–328, doi:10.1029/WR001i002p00325.

Brigaud, F., and G. Vasseur (1989), Mineralogy, porosity and fluid control on thermal conductivity of sedimentary rocks, *Geophys. J. Int.*, *98*(3), 525–542, doi:10.1111/j.1365-246X.1989.tb02287.x.

Bullard, E. (1954), The Flow of Heat through the Floor of the Atlantic Ocean, *Proc. R. Soc. Lond. Math. Phys. Eng. Sci.*, *222*(1150), 408–429, doi:10.1098/rspa.1954.0085.

Burton-Johnson, A., J. A. Halpin, J. M. Whittaker, F. S. Graham, and S. J. Watson (2017), A new heat flux model for the Antarctic Peninsula incorporating spatially variable upper crustal radiogenic heat production, *Geophys. Res. Lett.*, *44*(11), doi:10.1002/2017GL073596.

Cande, S. C., J. M. Stock, R. D. Müller, and T. Ishihara (2000), Cenozoic motion between East and West Antarctica, *Nature*, *404*(6774), 145–150, doi:10.1038/35004501.

Carslaw, H. S., and J. C. Jaeger (1947), *Conduction of heat in solids*, Oxford Clarendon Press.

Carson, C. J., S. McLaren, J. L. Roberts, S. D. Boger, and D. D. Blankenship (2014), Hot rocks in a cold place: high sub-glacial heat flow in East Antarctica, *J. Geol. Soc.*, *171*(1), 9–12, doi:10.1144/jgs2013-030.

Chaput, J., R. C. Aster, A. Huerta, X. Sun, A. Lloyd, D. Wiens, A. Nyblade, S. Anandakrishnan, J. P. Winberry, and T. Wilson (2014), The crustal thickness of West Antarctica, *J. Geophys. Res. Solid Earth*, *119*(1), 378–395, doi:10.1002/2013JB010642.

Christner, B. C. et al. (2014), A microbial ecosystem beneath the West Antarctic ice sheet, *Nature*, *512*(7514), 310–313, doi:10.1038/nature13667.

Christoffersen, P., M. Bougamont, S. P. Carter, H. A. Fricker, and S. Tulaczyk (2014), Significant groundwater contribution to Antarctic ice streams hydrologic budget, *Geophys. Res. Lett.*, *41*(6), 2014GL059250, doi:10.1002/2014GL059250.

Clauser, C., and E. Huenges (1995), Thermal conductivity of rocks and minerals, *Rock Phys. Phase Relat. Handb. Phys. Constants*, 105–126.

Clow, G. D., K. M. Cuffey, and E. D. Waddington (2012), High Heat-Flow Beneath the Central Portion of the West Antarctic Ice Sheet, *AGU Fall Meet. Abstr.*, *31*.

Comiso, J. C. (2000), Variability and Trends in Antarctic Surface Temperatures from In Situ and Satellite Infrared Measurements, *J. Clim.*, *13*(10), 1674–1696, doi:10.1175/1520-0442(2000)013<1674:VATIAS>2.0.CO;2.

Coney, P. J., and T. A. Harms (1984), Cordilleran metamorphic core complexes: Cenozoic extensional relics of Mesozoic compression, *Geology*, *12*(9), 550–554, doi:10.1130/0091-7613(1984)12<550:CMCCCE>2.0.CO;2.

Corr, H. F. J., and D. G. Vaughan (2008), A recent volcanic eruption beneath the West Antarctic ice sheet, *Nat. Geosci.*, *1*(2), 122–125, doi:10.1038/ngeo106.

Cuffey, K., and W. S. B. Paterson (2010), *The physics of glaciers*, 4th ed., Butterworth-Heinemann/Elsevier, Burlington, MA.

Davies, J. H., and D. R. Davies (2010), Earth's surface heat flux, *Solid Earth*, *1*(1), 5–24.

Davis, E. E. et al. (1992), FlankFlux: an experiment to study the nature of hydrothermal circulation in young oceanic crust, *Can. J. Earth Sci.*, *29*(5), 925–952, doi:10.1139/e92-078.

Davis, E. E., and A. T. Fisher (2011), Heat Flow, Seafloor: Methods and Observations, in *Encyclopedia of Solid Earth Geophysics*, edited by H. K. Gupta, pp. 582–591, Springer Netherlands.

Davis, E. E., K. Wang, J. He, D. S. Chapman, H. Villinger, and A. Rosenberger (1997), An unequivocal case for high Nusselt number hydrothermal convection in sediment-buried igneous oceanic crust, *Earth Planet. Sci. Lett.*, *146*(1), 137–150, doi:10.1016/S0012-821X(96)00212-9.

Decesari, R., D. Wilson, B. Luyendyk, and M. Faulkner (2007), Cretaceous and Tertiary extension throughout the Ross Sea, Antarctica, in Antarctica: A Keystone in a Changing World, in *Online Proceedings of the 11ISAES*, vol. Short Research Paper 098, edited by A. K. Cooper, C. R. Raymond, et al., p. 6 p.

Dziadek, R., K. Gohl, A. Diehl, and N. Kaul (2017), Geothermal heat flux in the Amundsen Sea sector of West Antarctica: New insights from temperature measurements, depth to the bottom of the magnetic source estimation, and thermal modeling, *Geochem. Geophys. Geosystems*, doi:10.1002/2016GC006755.

Engelhardt, H. (2004a), Ice temperature and high geothermal flux at Siple Dome, West Antarctica, from borehole measurements, *J. Glaciol.*, *50*(169), 251–256, doi:10.3189/172756504781830105.

Engelhardt, H. (2004b), Thermal regime and dynamics of the West Antarctic ice sheet, *Ann. Glaciol.*, *39*(1), 85–92, doi:10.3189/172756404781814203.

Favier, L., and F. Pattyn (2015), Antarctic ice rise formation, evolution, and stability, *Geophys. Res. Lett.*, *42*(11), doi:10.1002/2015GL064195.

Fisher, A. T., K. Becker, I. T. N. Narasimhan, M. G. Langseth, and M. J. Mottl (1990), Passive, off-axis convection through the southern flank of the Costa Rica Rift, *J. Geophys. Res. Solid Earth*, *95*(B6), 9343–9370, doi:10.1029/JB095iB06p09343.

Fisher, A. T. et al. (2003), Hydrothermal recharge and discharge across 50 km guided by seamounts on a young ridge flank, *Nature*, *421*(6923), 618–621, doi:10.1038/nature01352.

Fisher, A. T., and R. N. Harris (2010), Using seafloor heat flow as a tracer to map subseafloor fluid flow in the ocean crust, *Geofluids*, doi:10.1111/j.1468-8123.2009.00274.x.

Fisher, A. T., K. D. Mankoff, S. M. Tulaczyk, S. W. Tyler, N. Foley, and the W. S. Team (2015), High geothermal heat flux measured below the West Antarctic Ice Sheet, *Sci. Adv.*, *1*(6), doi:10.1126/sciadv.1500093.

Foster, T. D. (1978), Temperature and salinity fields under the Ross Ice Shelf, *Antarct. J*, *13*, 81–82.

Fretwell, P. et al. (2013), Bedmap2: improved ice bed, surface and thickness datasets for Antarctica, *The Cryosphere*, *7*(1), 375–393, doi:10.5194/tc-7-375-2013.

Fudge, T. J., E. J. Steig, B. R. Markle, S. W. Schoenemann, and Q. Ding (2013), Onset of deglacial warming in West Antarctica driven by local orbital forcing, *Nature*, *500*(7463), 440–444, doi:10.1038/nature12376.

Gades, A. M., C. F. Raymond, H. Conway, and R. W. Jacobel (2000), Bed properties of Siple Dome and adjacent ice streams, West Antarctica, inferred from radio-echo sounding measurements, *J. Glaciol.*, *46*(152), 88–94, doi:10.3189/172756500781833467.

Gangadhara Rao, M., and D. N. Singh (1999), A generalized relationship to estimate thermal resistivity of soils, *Can. Geotech. J.*, *36*(4), 767–773, doi:10.1139/t99-037.

Hasterok, D., and D. S. Chapman (2011), Heat production and geotherms for the continental lithosphere, *Earth Planet. Sci. Lett.*, *307*(1–2), 59–70, doi:10.1016/j.epsl.2011.04.034.

Heesemann, M., H. Villinger, A. T. Fisher, A. M. Trehu, and S. Witte (2006), *Testing and deployment of the new APC3 tool to determine in situ temperature while piston coring*, Proceedings of the IODP, edited by M. Riedel, T. S. Collett, M. J. Malone, and Expedition 311 Scientists, Integrated Ocean Drilling Program Management International Inc., College Station, TX.

Hirschmann, M. M. (2000), Mantle solidus: Experimental constraints and the effects of peridotite composition, *Geochem. Geophys. Geosystems*, *1*(10), 1042, doi:10.1029/2000GC000070.

IOC, SCOR, and IAPSO (2010), The international thermodynamic - 2010: Calculation and use of thermodynamic properties, *Intergov. Oceanogr. Comm. Man. Guid.*, *56*, 196.

Jørgensen, B. B., and A. Boetius (2007), Feast and famine — microbial life in the deep-sea bed, *Nat. Rev. Microbiol.*, *5*(10), 770–781, doi:10.1038/nrmicro1745.

Kingslake, J., R. C. A. Hindmarsh, G. Aðalgeirsdóttir, H. Conway, H. F. J. Corr, F. Gillet-Chaulet, C. Martín, E. C. King, R. Mulvaney, and H. D. Pritchard (2014), Full-depth englacial vertical ice sheet velocities measured using phase-sensitive radar, *J. Geophys. Res. Earth Surf.*, *119*(12), 2014JF003275, doi:10.1002/2014JF003275.

Lachenbruch, A. H., and J. H. Sass (1978), 9: Models of an extending lithosphere and heat flow in the Basin and Range province, *Geol. Soc. Am. Mem.*, *152*, 209–250, doi:10.1130/MEM152-p209.

Lachenbruch, A. H., J. H. Sass, R. J. Munroe, and T. H. Moses (1976), Geothermal setting and simple heat conduction models for the Long Valley Caldera, *J. Geophys. Res.*, *81*(5), 769–784, doi:10.1029/JB081i005p00769.

LeMasurier, W. E. (1990), Late Cenozoic Volcanism on the Antarctic Plate: An Overview, in *Volcanoes of the Antarctic Plate and Southern Oceans*, edited by W. E. LeMasurier, J. W. Thomson, P. E. Baker, P. R. Kyle, P. D. Rowley, J. L. Smellie, and W. J. Verwoerd, pp. 1–17, American Geophysical Union.

LeMasurier, W. E. (2008), Neogene extension and basin deepening in the West Antarctic rift inferred from comparisons with the East African rift and other analogs, *Geology*, *36*(3), 247–250, doi:10.1130/G24363A.1.

Lough, A. C., D. A. Wiens, C. Grace Barcheck, S. Anandakrishnan, R. C. Aster, D. D. Blankenship, A. D. Huerta, A. Nyblade, D. A. Young, and T. J. Wilson (2013), Seismic detection of an active subglacial magmatic complex in Marie Byrd Land, Antarctica, *Nat. Geosci.*, *6*(12), 1031–1035, doi:10.1038/ngeo1992.

Lythe, M. B., and D. G. Vaughan (2001), BEDMAP: A new ice thickness and subglacial topographic model of Antarctica, *J. Geophys. Res. Solid Earth*, *106*(B6), 11335–11351, doi:10.1029/2000JB900449.

Mancktelow, N. S., and B. Grasemann (1997), Time-dependent effects of heat advection and topography on cooling histories during erosion, *Tectonophysics*, *270*(3–4), 167–195, doi:10.1016/S0040-1951(96)00279-X.

Martín, C., R. C. A. Hindmarsh, and F. J. Navarro (2006), Dating ice flow change near the flow divide at Roosevelt Island, Antarctica, by using a thermomechanical model to predict radar stratigraphy, *J. Geophys. Res. Earth Surf.*, *111*, doi:10.1029/2005JF000326.

Matsuoka, K. et al. (2015), Antarctic ice rises and rumples: Their properties and significance for ice-sheet dynamics and evolution, *Earth-Sci. Rev.*, *150*, 724–745, doi:10.1016/j.earscirev.2015.09.004.

Maule, C. F. et al. (2005), Heat Flux Anomalies in Antarctica Revealed by Satellite Magnetic Data, *Science*, *309*(5733), 464–467, doi:10.1126/science.1106888.

Morin, R., and A. J. Silva (1984), The effects of high pressure and high temperature on some physical properties of ocean sediments, *J. Geophys. Res. Solid Earth*, *89*(B1), 511–526, doi:10.1029/JB089iB01p00511.

Muto, A., K. Christianson, H. J. Horgan, S. Anandakrishnan, and R. B. Alley (2013), Bathymetry and geological structures beneath the Ross Ice Shelf at the mouth of Whillans Ice Stream, West Antarctica, modeled from ground-based gravity measurements: Grounding zone and subglacial conditions, *J. Geophys. Res. Solid Earth*, *118*(8), 4535–4546, doi:10.1002/jgrb.50315.

Näslund, J. O., L. Rodhe, J. L. Fastook, and P. Holmlund (2003), New ways of studying ice sheet flow directions and glacial erosion by computer modelling—examples from Fennoscandia, *Quat. Sci. Rev.*, *22*(2–4), 245–258, doi:10.1016/S0277-3791(02)00079-3.

Paterson, W. S. B. (1976), Vertical Strain-rate Measurements in an Arctic Ice Cap and deductions from them, *J. Glaciol.*, *17*(75), 3–12, doi:10.1017/S0022143000030665.

Pittard, M. L., B. K. Galton-Fenzi, J. L. Roberts, and C. S. Watson (2016), Organization of ice flow by localized regions of elevated geothermal heat flux, *Geophys. Res. Lett.*, *43*(7), doi:10.1002/2016GL068436.

Pollack, H. N., S. J. Hurter, and J. R. Johnson (1993), Heat flow from the Earth's interior: Analysis of the global data set, *Rev. Geophys.*, *31*(3), 267–280, doi:10.1029/93RG01249.

Price, S. F., H. Conway, and E. D. Waddington (2007), Evidence for late Pleistocene thinning of Siple Dome, West Antarctica, *J. Geophys. Res. Earth Surf.*, *112*(F3), F03021, doi:10.1029/2006JF000725.

Raymond, C. F. (1983), Deformation in the Vicinity of Ice Divides, *J. Glaciol.*, *29*(103), 357–373, doi:10.3198/1983JoG29-103-357-373.

Raymond, C. (1996), Shear margins in glaciers and ice sheets, *J. Glaciol.*, *42*(140), 90–102.

Reiter, M., C. L. Edwards, H. Hartman, and C. Weidman (1975), Terrestrial Heat Flow along the Rio Grande Rift, New Mexico and Southern Colorado, *Geol. Soc. Am. Bull.*, *86*(6), 811–818, doi:10.1130/0016-7606(1975)86<811:THFATR>2.0.CO;2.

Rignot, E., D. G. Vaughan, M. Schmeltz, T. Dupont, and D. MacAyeal (2002), Acceleration of Pine Island and Thwaites Glaciers, West Antarctica, *Ann. Glaciol.*, *34*(1), 189–194, doi:10.3189/172756402781817950.

Rignot, E., G. Casassa, P. Gogineni, W. Krabill, A. Rivera, and R. Thomas (2004), Accelerated ice discharge from the Antarctic Peninsula following the collapse of Larsen B ice shelf, *Geophys. Res. Lett.*, *31*(18), doi:10.1029/2004GL020697.

Rignot, E., J. Mouginot, and B. Scheuchl (2011), Ice Flow of the Antarctic Ice Sheet, *Science*, *333*(6048), 1427–1430, doi:10.1126/science.1208336.

Robin, G. D. Q. (1955), Ice Movement and Temperature Distribution in Glaciers and Ice Sheets, *J. Glaciol.*, *2*(18), 523–532, doi:10.3189/002214355793702028.

Scambos, T. A., T. M. Haran, M. A. Fahnestock, T. H. Painter, and J. Bohlander (2007), MODIS-based Mosaic of Antarctica (MOA) data sets: Continent-wide surface morphology and snow grain size, *Remote Sens. Environ.*, *111*(2–3), 242–257, doi:10.1016/j.rse.2006.12.020.

Schroeder, D. M., D. D. Blankenship, D. A. Young, and E. Quartini (2014), Evidence for elevated and spatially variable geothermal flux beneath the West Antarctic Ice Sheet, *Proc. Natl. Acad. Sci.*, doi:10.1073/pnas.1405184111.

Shapiro, N. M., and M. H. Ritzwoller (2004), Inferring surface heat flux distributions guided by a global seismic model: particular application to Antarctica, *Earth Planet. Sci. Lett.*, *223*(1–2), 213–224, doi:10.1016/j.epsl.2004.04.011.

Seront, B., T.-F. Wong, J. S. Caine, C. B. Forster, R. L. Bruhn, and J. T. Fredrich (1998), Laboratory characterization of hydromechanical properties of a seismogenic normal fault system, *J. Struct. Geol.*, *20*(7), 865–881, doi:10.1016/S0191-8141(98)00023-6.

Siegert, M. J., and J. A. Dowdeswell (1996), Spatial variations in heat at the base of the Antarctic ice sheet from analysis of the thermal regime above subglacial lakes, *J. Glaciol.*, *42*(142), 501–509.

Spinelli, G. A., and A. T. Fisher (2004), Hydrothermal circulation within topographically rough basaltic basement on the Juan de Fuca Ridge flank, *Geochem. Geophys. Geosystems*, *5*(2), doi:10.1029/2003GC000616.

Swanberg, C. A. (1972), Vertical distribution of heat generation in the Idaho batholith, *J. Geophys. Res.*, *77*(14), 2508–2513, doi:10.1029/JB077i014p02508.

Trey, H., A. K. Cooper, G. Pellis, B. della Vedova, G. Cochrane, G. Brancolini, and J. Makris (1999), Transect across the West Antarctic rift system in the Ross Sea, Antarctica, *Tectonophysics*, *301*(1–2), 61–74, doi:10.1016/S0040-1951(98)00155-3.

Tulaczyk, S., B. Kamb, and H. F. Engelhardt (2001), Estimates of effective stress beneath a modern West Antarctic ice stream from till preconsolidation and void ratio, *Boreas*, *30*(2), 101–114, doi:10.1111/j.1502-3885.2001.tb01216.x.

Tulaczyk, S. et al. (2014), WISSARD at Subglacial Lake Whillans, West Antarctica: scientific operations and initial observations, *Ann. Glaciol.*, *55*(65), 51–58, doi:10.3189/2014AoG65A009.

Vaughan, D. G., J. L. Bamber, M. Giovinetto, J. Russell, and A. P. R. Cooper (1999), Reassessment of Net Surface Mass Balance in Antarctica, *J. Clim.*, *12*(4), 933–946, doi:10.1175/1520-0442(1999)012<0933:RONSMB>2.0.CO;2.

Vilà, M., M. Fernández, and I. Jiménez-Munt (2010), Radiogenic heat production variability of some common lithological groups and its significance to lithospheric thermal modeling, *Tectonophysics*, *490*(3–4), 152–164, doi:10.1016/j.tecto.2010.05.003.

Villinger, H., I. Grevemeyer, N. Kaul, J. Hauschild, and M. Pfender (2002), Hydrothermal heat flux through aged oceanic crust: where does the heat escape?, *Earth Planet. Sci. Lett.*, *202*(1), 159–170, doi:10.1016/S0012-821X(02)00759-8.

Vogel, S. W., and S. Tulaczyk (2006), Ice-dynamical constraints on the existence and impact of subglacial volcanism on West Antarctic ice sheet stability, *Geophys. Res. Lett.*, *33*(23), doi:10.1029/2006GL027345.

Von Herzen, R., and A. E. Maxwell (1959), The measurement of thermal conductivity of deep-sea sediments by a needle-probe method, *J. Geophys. Res.*, *64*(10), 1557–1563, doi:10.1029/JZ064i010p01557.

Weertman, J. (1964), The theory of glacier sliding, *J. Glaciol.*, *5*, 287–303.

Wilson, D. S., S. S. R. Jamieson, P. J. Barrett, G. Leitchenkov, K. Gohl, and R. D. Larter (2012), Antarctic topography at the Eocene–Oligocene boundary, *Palaeogeogr. Palaeoclimatol. Palaeoecol.*, *335–336*, 24–34, doi:10.1016/j.palaeo.2011.05.028.

York, D., N. M. Evensen, M. L. Martínez, and J. D. B. Delgado (2004), Unified equations for the slope, intercept, and standard errors of the best straight line, *Am. J. Phys.*, *72*(3), 367–375, doi:10.1119/1.1632486.

Zagorodnov, V., O. Nagornov, T. A. Scambos, A. Muto, E. Mosley-Thompson, E. C. Pettit, and S. Tyuflin (2012), Borehole temperatures reveal details of 20th century warming at Bruce Plateau, Antarctic Peninsula, *The Cryosphere*, *6*(3), 675–686, doi:10.5194/tc-6-675-2012.

Zumberge, M. A., D. H. Elsberg, W. D. Harrison, E. Husmann, J. L. Morack, E. C. Pettit, and E. D. Waddington (2002), Measurement of vertical strain and velocity at Siple Dome, Antarctica, with optical sensors, *J. Glaciol.*, *48*(161), 217–225, doi:10.3189/172756502781831421.

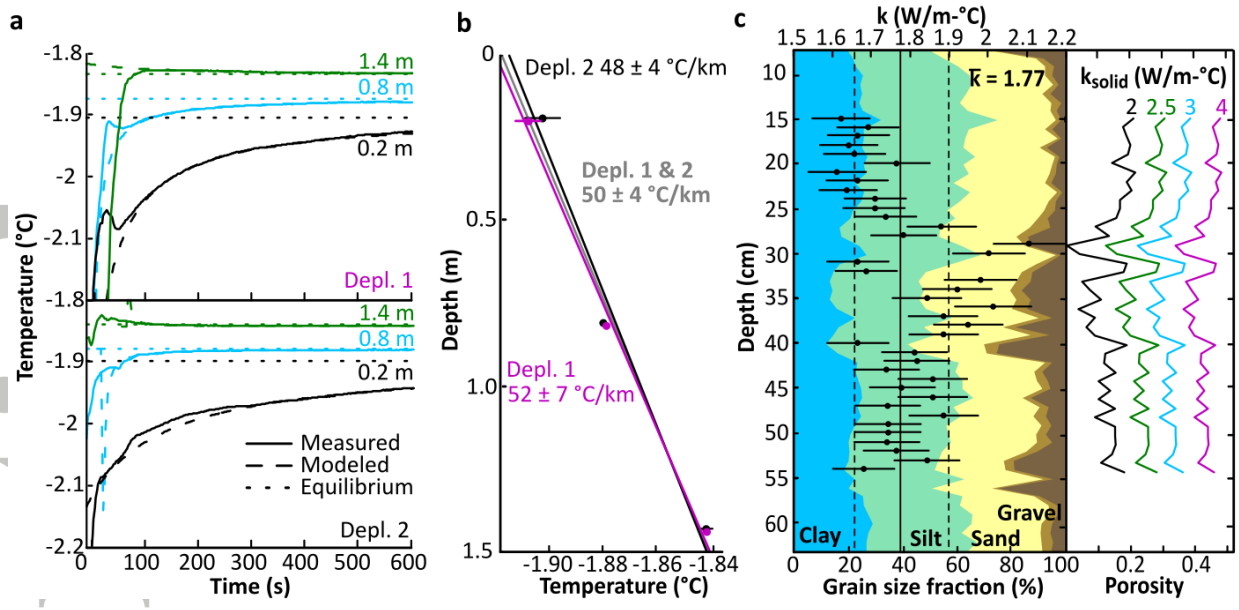

Figure 1. Temperature and thermal conductivity data from the WGZ. **a.** Temperature records for each sensor (depth in sediments labeled) during two geothermal probe deployments starting at the time of sediment penetration. **b.** Thermal gradient for each deployment and for the combined dataset constrained by equilibrium temperatures ± 1 S.E. **c.** Thermal conductivity (k) of sediments with ±5% errors and combined harmonic mean (labeled, solid vertical line) ± 1 S.D. (dashed lines). Cumulative grain size fractions indicated in color; gravel fraction is divided at 1 mm diameter. Inferred porosity for constant grain thermal conductivities (k_{solid}).

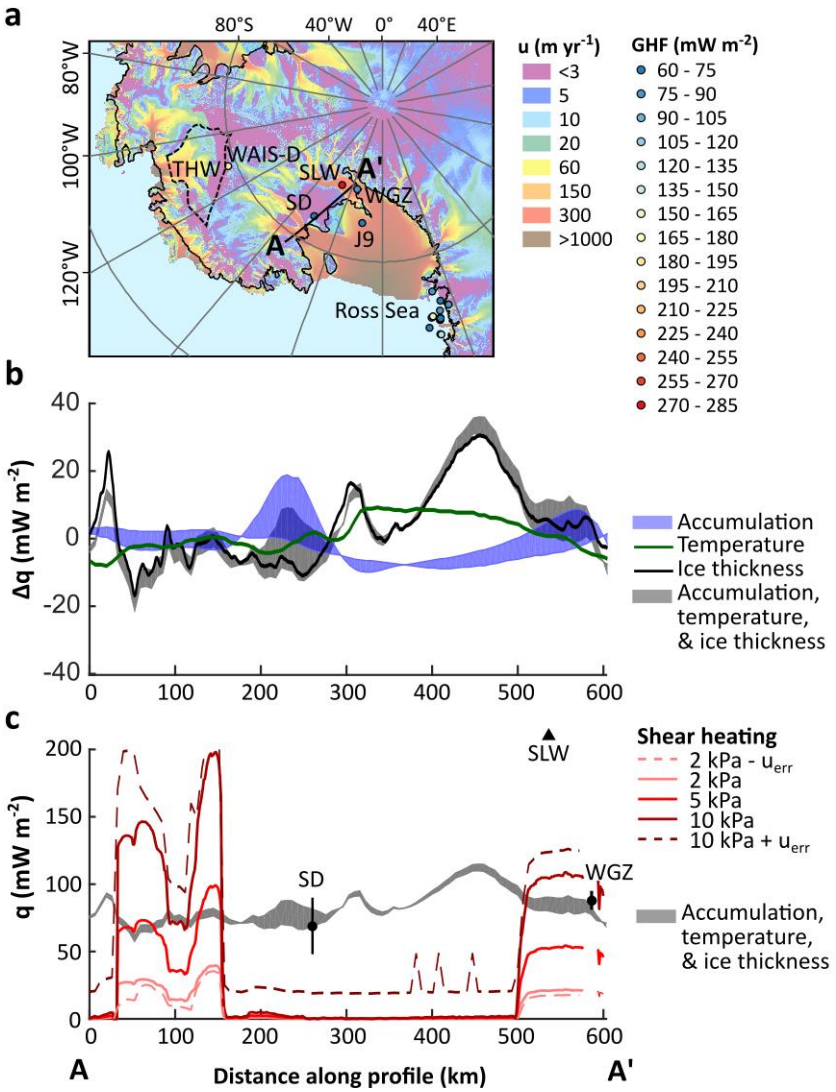

Figure 2. a. GHF measurements and estimates for West Antarctica [*Foster*, 1978; *Engelhardt*, 2004; *Fudge et al.*, 2013; *Fisher et al.*, 2015] and the Western Ross Sea region [*Morin et al.*, 2010 and references therein; *Schröder et al.*, 2011] overlain on ice velocity [*Rignot et al.*, 2011]. Grounding line outlined in black [*Bindschadler et al.*, 2011]. Profile line (A-A') shown in black. Extent of GHF estimates below Thwaites Glacier (THW, dashed line) [*Schroeder et al.*, 2014]. **b.** Estimates of spatial variability in heat conduction and production along the profile line shown in (a), as difference from mean conductive heat flux along that profile (79 mW m^{-2}). **c.** Shear heat flux estimates calculated from ice velocity and associated errors. GHF measurements and estimates close to the profile line are plotted (mean ± 1 S.E., SLW value lies off-axis).

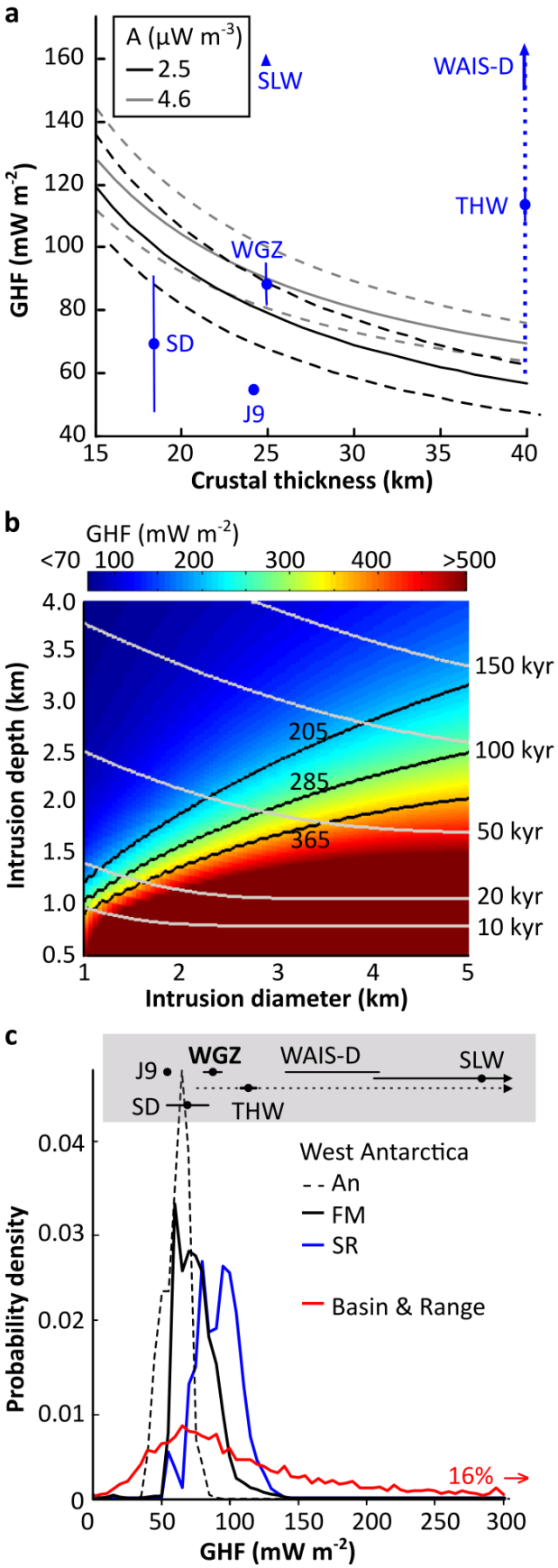

Figure 3. a. Analytical model for GHF based on Fox Maule *et al.* [2005] (black and grey lines) compared with GHF measurements and estimates (blue) as a function of magnetic crustal thickness. The SLW value lies well above the plot. Dotted lines show the envelope of

±15% variation in crustal thermal conductivity from 2.8 W $m^{-1}°C^{-1}$. **b.** GHF anomaly due to modeled magmatic intrusions with cubic geometry. Intrusion depths are the distance from the surface of the crust to top of the intrusion. GHF values are the maximum achieved at the surface over the center of the intrusion. Black contours represent mean ± 1 S.E bounds on GHF at SLW. Grey contours mark the time since emplacement at which the maximum GHF values plotted are achieved. **c.** Probability density functions of GHF models for West Antarctica [*Shapiro and Ritzwoller*, 2004; Fox *Maule et al.*, 2005; *An et al.*, 2015] and GHF measurements in the Basin and Range Province, USA, 16% of which exceed 300 mW m^{-2} [*National Geothermal Data System*]. **a and c.** GHF measurements and estimates for West Antarctica plotted as mean ± 1 S.E., where available (references in Fig. 2). GHF estimates below Thwaites Glacier (THW), shown in Fig. 3a, plotted as mean, ± 1 S.D. (solid line), and the full range of THW values (dotted line) which extends off-axis to 375 mW m^{-2} [*Schroeder et al.*, 2014].

Table 1. Observational constraints on GHF variability and candidate explanations.

	Magnitude of GHF difference (mW m^{-2})	**Lateral extent of GHF difference (km)**
Observations (SLW-WGZ)	197 ± 85	108
Observations (WGZ-J9)	33 ± 7	228
Candidate explanations		
Hydrothermal circulation	1000s	0.1 – 100s
Magmatic intrusion	1000s	<10
Crustal thickness variability	≤60	>130
Thermal conductivity variability	<30	>1
Radiogenic heat production	≤18	<20
Lithospheric extension	≤10	≥75
Erosion	<4	10 – 200